6

Phase transitions

In the present chapter we shall discuss the consequences the finite number of particles have in the phenomenon of pairing phase transition in atomic nuclei. Finite size effects give rise to fluctuations of the pairing gap and thus of the correlation length (order parameter) ξ. Because ξ is much larger than the size of the nucleus, it comes as no surprise that in describing the phase transition in the small-particle superconductors one doesn't need the non-analytic functions necessary to account for the condensation in infinite systems. On the other hand, the phenomena in both systems are closely related and, in a system like the nucleus, we have the possibility of studying the transition in terms of the spectrum of individual states. Thus the transition from a pair-correlated to a normal system with increasing angular momentum involves the coupling between rotational bands associated with the ground state and with excited (few quasiparticle) states.

Because all the transitions we shall treat are connected with level crossings at zero temperature, it is more appropriate to talk about quantal phase transitions (see Sachdev (1999)).

The variation of the moment of inertia $\mathcal{I}$ of rotational bands with angular momentum provides one clue to the variation of the pairing gap with angular momentum. This is because the moment of inertia has a simple monotonic dependence on Δ. In characterizing a superfluid nucleus the moment of inertia $\mathcal{I}$ of the rotational bands and the energy of the lowest non-collective excitations $2E_\nu$ play a central role. Bohr and Mottelson (1975, equation (4.128)) have given a qualitative estimate of the effect of pair correlations on the moment of inertia which depends on a dimensionless parameter $x \sim \beta_2\hbar\omega_0/2\Delta$ where β_2 is the quadrupole deformation of the system, $\hbar\omega_0 \sim 41/A^{1/3}$ MeV is the energy between major shells in the single-particle potential, and Δ is the pairing gap. Their expression for the relation between the rigid moment of inertia $\mathcal{I}_{\text{rig}}$ and the actual moment of inertia of a deformed nucleus is $\mathcal{I} = \mathcal{I}_{\text{rig}}(1 - g(x))$

117

where

$$g(x) \approx \frac{\ln\left(x + \sqrt{1 + x^2}\right)}{x\sqrt{1 + x^2}}.$$

The moment of inertia tends to the rigid value when the pairing is weak and decreases as Δ increases ($x \approx \beta_2 \hbar \omega_0 / 2\Delta$). For typical cases ($A = 160$, $\beta_2 \sim 0.3$, $\hbar \omega_0 \sim 7.5$, $\Delta \sim 0.9\,\mathrm{MeV}$) one obtains $x \sim 1.25$, and $g(x) \sim 0.5$. However, both $\mathcal{I}$ and E_ν are strongly dependent on the shape of the nucleus, which is modified by the rotation of the system as a whole, making it difficult to extract the order parameter from the changes observed in these quantities.

A better probe is the transfer of two nucleons as a function of the angular momentum. In fact, as already discussed in Chapters 4 and 5, the ratio of the two-nucleon transfer differential cross-section between the ground states of superfluid nuclei, normalized with respect to the DWBA differential cross-section calculated making use of a form factor describing the motion of two uncorrelated particles in a single j-orbit typical of the mass region, is approximately given by $(\Delta/G)^2$ where G is the pairing coupling constant.

New possibilities have been opened by the observation of tunnelling between different minima of the potential-energy surface, which displays a very strong dependence on the rotational frequency. The tunnelling probability depends exponentially on the pairing gap, making such measurements extremely sensitive to changes of Δ as a function of I. The tunnelling probability from a deformed to a superdeformed configuration (see Section 6.5) can be written in the WKB approximation, assuming the barrier is well described by an inverted parabola as a function of the deformation, as (see Chapter 7)

$$P \sim \exp\left[-\frac{2\pi(E_\mathrm{B} - E)}{\hbar\sqrt{C/D}}\right].$$

The quantity E_B is the height of the barrier, E the (zero point) energy of the system in the deformed minimum, while D and C are the tunnelling mass parameter of the system and the curvature of the parabola. In Section 7.1.1 it will be shown that $D \propto \Delta^{-2}$ for a superfluid nucleus.

In Sections 6.1–6.5 we discuss the general properties of the pairing phase transition as a function of I, paying special attention to the energies, alignments (derivative of the energies with respect to angular momenta) and moments of inertia. The dependence of the moment of inertia on pair correlations is discussed in Section 6.2.1 to obtain an estimate of the critical angular momentum for pair collapse. In Section 6.5 we discuss the role played by pairing in the tunnelling between superdeformed and normal deformed nuclei, while in the

last section we discuss the role that pairing fluctuations play in the rotation of nuclei.

6.1 The experimental situation

There are two mechanisms by which the nucleus can generate high angular momentum: single-particle alignment along a common axis or by a collective rotation of the nucleus as a whole. This is illustrated in Fig. 6.1, where level schemes of ^{158}Er and ^{147}Gd are shown. The ^{158}Er scheme is quite regular and the dominant behaviour is collective rotation of a body displaying prolate deformation. The spectrum of ^{147}Gd is very irregular, with complicated decay pathways and isomeric states. Its dominant behaviour is very likely single-particle alignment.

In spite of differences, both of these schemes contain elements of the other type of behaviour. In particular, there are irregularities in the ^{158}Er rotational pattern at spins around 16 and 26. In fact, as the nucleus de-excites from a high
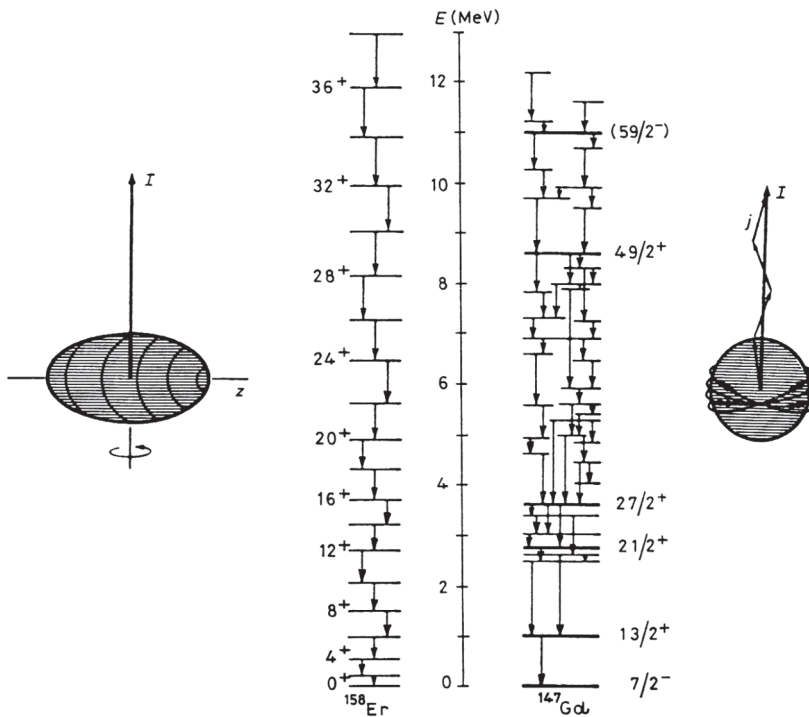
Figure 6.1. Level scheme for ^{158}Er and ^{147}Gd, together with illustrations of the dominant source of angular momentum for each case (from Stephens (1985)).
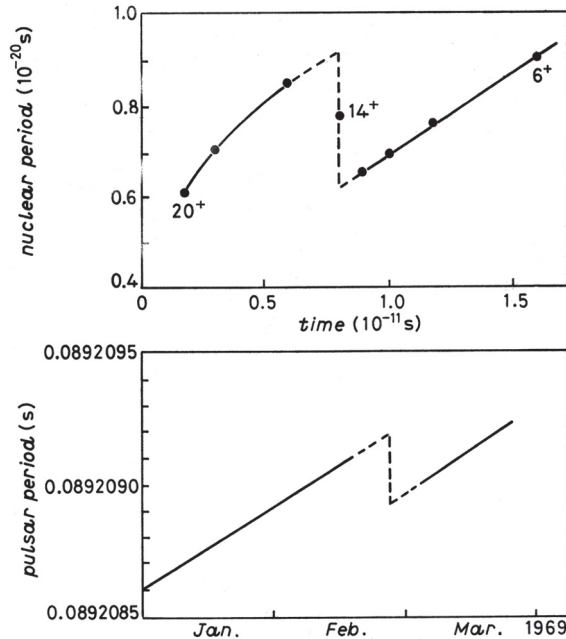
Figure 6.2. Plots of the rotational period against time for the nucleus [158]Er (top) and the pulsar Vela (bottom) (from Stephens (1985)).

initial spin, the regular increase of the nuclear period (slowing-down) is interrupted occasionally by rather marked decreases. These correspond to internal rearrangements, 'nuclear quakes', and are generally called 'backbends'. One may compare them to another type of quakes – 'star-quakes'. Neutron stars or 'pulsars' are also rapidly rotating systems that are slowing down (Chapter 1). Occasionally they too display sudden speed ups of the rotational motion called 'glitches' (see Anderson *et al.* (1982), Ruderman (1972), Shapiro and Teukolsky (1983), Pines *et al.* (1992)).

It is quite common for rapidly rotating objects to modify their internal structure and thus their moments of inertia, and that these modifications revert back, often in sudden jumps of the rotational period, as the system slows down. The interesting question for each system has to do with the nature of the internal modification. The slowing-down of the nucleus [158]Er below spin 20 is compared with the pulsar Vela in Fig. 6.2. The behaviours are quite similar, though the percentage change in the nuclear case is much larger. The pulsar glitches are not too well understood at present – early explanations had to do with a sudden breaking of the solid crust on the neutron star, but more recent ones involve vortices in the flow pattern (see e.g. Epstein and Baym (1988), Pizzochero *et al.* (1997), Alpar (1977, 1998), Donati and Pizzochero (2003)). The nuclear glitch

is due to the sudden pairing of two high-j particles. In the case of this first backbend in ^{158}Er, the particles are $i_{13/2}$ neutrons. Above $I \sim 14$ this pair of aligned particles contributes $10\hbar$ along the rotation axis, but this is lost below $I \sim 14$ when the particles suddenly couple to spin nearly zero (decoupling) and begin to participate in the pairing correlations. The angular momentum has to be made up by the collective rotation, which must speed up, thereby decreasing the period.

Such a behaviour is now well studied in nuclei around ^{158}Er, and the change described above corresponds to a crossing of two rotational bands (Stephens and Simon (1972)). A band with two aligned $i_{13/2}$ neutrons crosses the ground-state band, which has all particles participating in the pairing correlations (pairing vacuum). Thus the discontinuity actually corresponds to a shift into another band, though the mixing between these bands gives collective enhancement to the transition connecting the bands, often to the point where they are stronger than the 'in-band' transitions at the crossing. The energy of the aligned band relative to the ground band gradually decreases with increasing spin because of the Coriolis interaction. Just as a gyroscope will attempt to align its rotation axis with that of its rotating frame, so a pair of high-j particles tends to align its rotation axis (angular momentum) with that of the rotating nucleus, thereby decreasing its energy relative to a band without such an alignment.

The shift in angular momentum between the orbital motion of individual particles and the collective rotation of the nucleus is illustrated in Fig. 6.3, where the top figure is the moment of inertia plotted against angular frequency ($\hbar\omega = E_\gamma/2$) for a nucleus ^{158}Er. The sharp increases in the moment of inertia due to the alignments are apparent, the first one giving rise to a 'backbending' as the sequence shifts bands and the second to an 'upbend'. In the centre of Fig. 6.3, spin is plotted against angular frequency. The members of the three different bands fall rather clearly on separate lines, and the difference in spin between the lines at a given frequency represents the difference in aligned angular momentum, Δi, between the bands at that frequency. The $i_{13/2}$ band has about $10\hbar$ units on angular momentum aligned relative to the ground band of ^{158}Er. The next higher band has two more particles aligned (four-quasiparticle state), which are believed to be $h_{11/2}$ protons, and the additional Δi is about $7\hbar$. Both the spin and the angular frequency in Fig. 6.3 are directly measurable quantities. Another is the interaction of the two bands as they cross. A strong interaction means heavy mixing of the bands and a 'smoothed-out' crossing, whereas weak interactions are associated with sudden sharp crossings. The crossing of rotational bands is illustrated in Fig. 6.4 where the energy levels of ^{160}Yb are plotted against spin. In addition to the two bands crossing along the yrast sequence, there are many band crossings in the levels above. In the case of ^{158}Er there are three band crossings in the first few MeV of excitation. The crossing points occur near the backbends or upbends in Fig. 6.3.
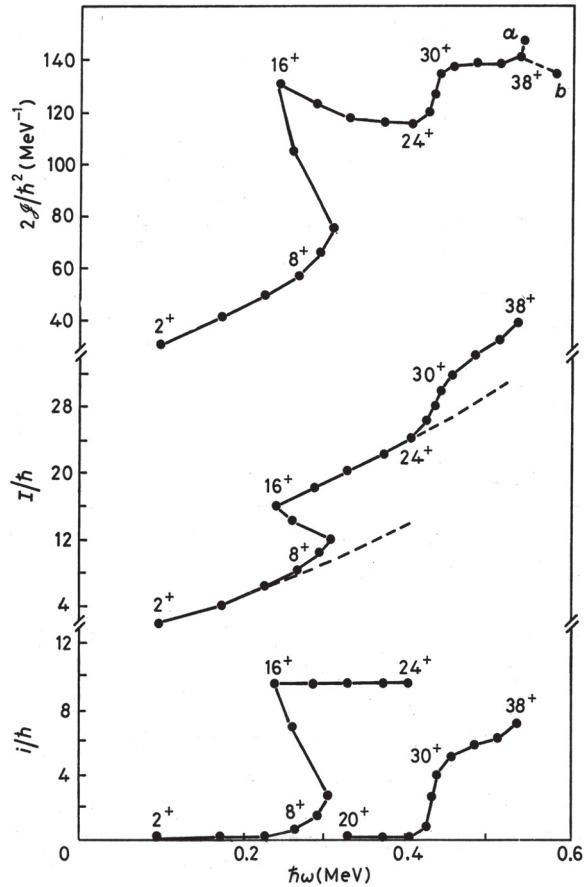
Figure 6.3. Plots of the moment of inertia (top), spin (middle) and spin alignment (bottom) against the rotational frequency for the yrast sequence in ^{158}Er (Yrast states are the states with lowest energy for each angular momentum). The angular velocity is obtained from the measured γ-ray energies in the collective rotational band by $2\hbar\omega = E_\gamma$. The moment of inertia is defined by $\mathcal{I} = I/\omega$. The experimental alignment in the lower part of the figure is defined by $i(\omega) = I - I_s(\omega)$ where $I_s(\omega)$ is the angular momentum of a reference band indicated by the dashed curves in the middle part of the figure. It is fitted to the smoothly varying parts of the curve of angular momentum $I(\omega)$ (after Stephens (1985)).

6.2 Static pairing correlations: the BCS theory of pairing phase transitions in strongly rotating nuclei

The nucleon orbitals in a static deformed potential are twofold degenerate, corresponding to a time reversal of their motion (Kramers degeneracy). This situation for an axially symmetric prolate nucleus is illustrated at the top of Fig. 6.5. The angular momentum, j, of the nucleon has projections $\pm\Omega$ along the symmetry axis and, when occupied by two nucleons, results in total angular momentum
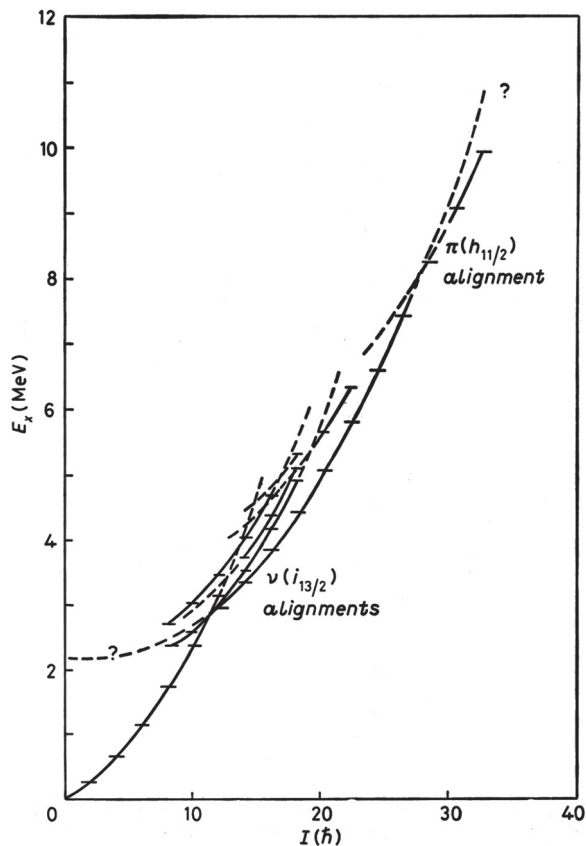
Figure 6.4. Rotational-band trajectories on an E against I plot for the levels of ^{160}Yb. The observed levels are indicated by the horizontal marks (after Stephens (1985)).

zero. Every orbital, characterized by j, Ω, can give rise to such a spin-zero pair. The nucleons in a filled orbital near the Fermi level can scatter as a pair into a nearby empty orbital, and the coherent scattering pattern that develops comprises the nuclear pairing correlation.

These pairing correlations affect the ability of the nucleus to generate angular momentum. In fact, insofar as the pairs are coupled to spin zero, they can contribute nothing towards generating angular momentum. This causes a reduction factor of 2–3 in the nuclear moment of inertia, which is given reasonably well by the BCS model (equation (3.91)). It follows that angular momentum will tend to weaken the pairing correlations, thus increasing the moment of inertia and reducing the rotational energy.

The mechanism of this weakening is the Coriolis force, which acts oppositely on the two members of the pair, lifting their degeneracy. Ultimately the Coriolis
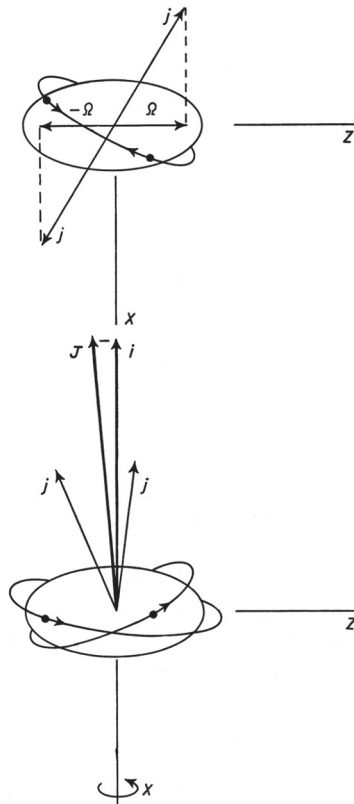
Figure 6.5. The two important coupling schemes in deformed nuclei. In the absence of rotation (top) particles with angular momentum j are in time-reversed orbits with projections $\pm\Omega$ along the symmetry (z)-axis. At high rotational frequencies the particles couple to a J, aligned as well as possible with the rotation (x)-axis, along which they have projection i (from Stephens (1985)).

force will align the particle angular momentum as well as possible with the rotation axis, as illustrated at the bottom of Fig. 6.5. This process is analogous to the effect of a magnetic field on the paired electrons in a superconductor.

6.2.1 Estimate of crossing frequency: gapless superconductivity

Pair correlations lead to a decrease in the rotational moment of inertia and, hence, to an increase in the rotational energy for given I. Thus, for sufficiently large rotational frequencies, the gain in energy associated with the pair correlation is upset by the increased rotational energy, and one expects (Mottelson and Valatin (1960), Bohr (1977)) a phase transition to normal nuclear matter (see Fig. 6.6).
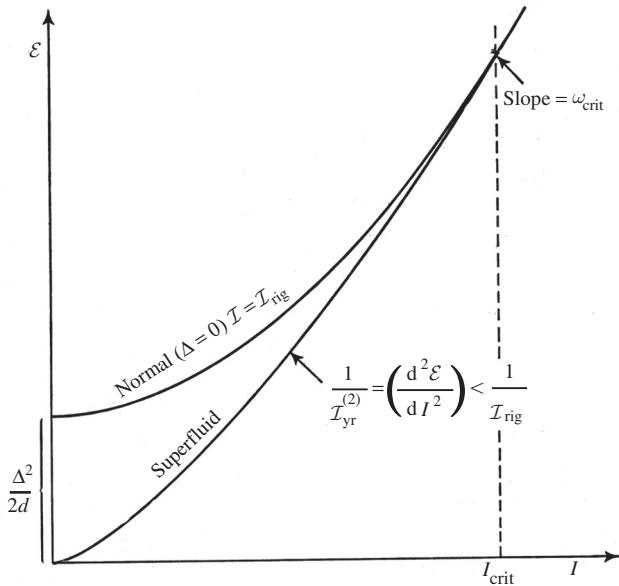
Figure 6.6. Schematic comparison between yrast lines for superfluid and normal systems (from Bohr and Mottelson (1981)). The quantity $\Delta^2/2d$ is the pairing correlation energy (see Section 3.5).

With pairing included, single-particle motion in a rotating potential can be described by a Hamiltonian of the form

$$H' = H_{\text{sp}} + V_{\text{pair}} - \lambda \hat{N} - \hbar \omega j_x, \tag{6.1}$$

with

$$H_{\text{sp}} - \lambda \hat{N} = \sum_{\nu>0} 2(\varepsilon_\nu - \lambda) a_\nu^\dagger a_\nu, \tag{6.2}$$

$$V_{\text{pair}} = -\Delta \sum_{\nu>0} (a_\nu^\dagger a_{\bar{\nu}}^\dagger + a_{\bar{\nu}} a_\nu), \tag{6.3}$$

$$j_x = \sum_{\nu_1 \nu_2} \langle \nu_2 | j_x | \nu_1 \rangle a_{\nu_2}^\dagger a_{\nu_1}, \tag{6.4}$$

where ν labels the eigenstates of H_{sp} and $\bar{\nu}$ is the time reverse of ν. The number operator is denoted by $\hat{N}$. The pair potential includes only the monopole term that creates and annihilates pairs of particles moving in single-particle states conjugate under time reversal. Additional terms in the pair potential may be present. The strength of the pair potential, as well as the shape of the nucleus, is a function of ω characterizing the equilibrium for given rotational frequency.

The Hamiltonian (6.1) is a bilinear form in the particle creation and annihilation operators $a^\dagger, a$ and can be brought to diagonal form by a linear

transformation to quasiparticle operators

$$\alpha_i^\dagger = \sum_\nu (U_{i\nu} a_\nu^\dagger - V_{i\nu} a_{\bar{\nu}}), \tag{6.5}$$

leading to

$$H' = \text{const} + \sum_i E_i' \alpha_i^\dagger \alpha_i. \tag{6.6}$$

The transformation (6.5) is a generalization of the more familiar one which applies to time-reversal-invariant potentials (Bohr and Mottelson (1974), Bohr (1977)). Essential new features are that the quasiparticle states no longer have the twofold degeneracy and that the quasiparticle energies E' can be smaller than Δ (in analogy to the situation in gapless superconductors (Goswami *et al.* (1967))).

We can see the new features most easily for a nucleus rotating about the symmetry axis. In this case, the eigenstates ν of H_{sp} are also eigenstates of j_x (with eigenvalue Ω). The quasiparticle transformation is now the usual one as for τ-invariant potentials

$$\begin{cases} \alpha_\nu^\dagger = U_\nu a_\nu^\dagger - V_\nu a_{\bar{\nu}}, \\ a_\nu^\dagger = U_\nu \alpha_\nu^\dagger + V_\nu \alpha_{\bar{\nu}}, \end{cases} \tag{6.7}$$

which leaves the operator j_x diagonal

$$j_x = \sum_\nu \Omega a_\nu^\dagger a_\nu = \sum_\nu \Omega \alpha_\nu^\dagger \alpha_\nu, \tag{6.8}$$

and the quasiparticle energies are

$$E_\nu' = \left((\varepsilon_\nu - \lambda)^2 + \Delta^2 \right)^{1/2} - \hbar\omega\Omega. \tag{6.9}$$

The quasiparticle spectrum (6.9) is illustrated schematically in Fig. 6.7. For an even number of particles, the quasiparticle vacuum ($v = 0$) is the lowest state for rotational frequencies that are smaller than the value for which the sum of the two lowest quasiparticle energies vanishes. For larger ω, this two-quasiparticle state becomes the lowest (so called 'yrast' state, i.e. the set of states that have the lowest energy for each angular momentum), until the next pair of quasiparticles has zero energy, after which the four-quasiparticle state moves to the yrast line, etc. The characteristic frequency ω_1 for the first of these crossings is of order

$$\omega_1 \sim \frac{\Delta}{\Omega_{\text{max}}}, \tag{6.10}$$
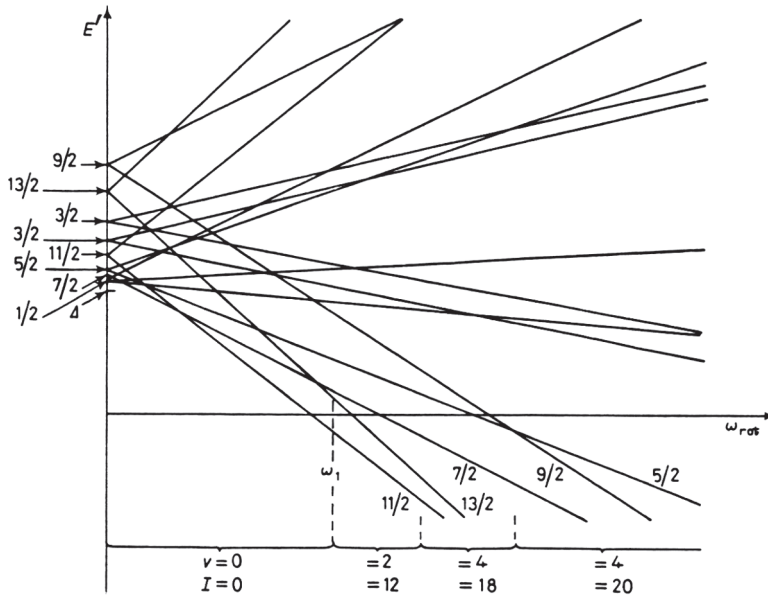
Figure 6.7. Quasiparticle energies E' corresponding to a schematic single-particle spectrum (from Bohr (1977)). Copyright © Società italiana di Fisica.

where $\Omega_{\max}(= j_{\max})$ is the largest single-particle angular momentum near the Fermi surface. Systematics obtained from experimental data are fitted well by an empirical relation (see equation (1.43))

$$\hbar\omega_1 \approx \frac{1.67\Delta}{j_1}.$$

Estimates for band crossings for some high-j shells are found in Garrett *et al.* (1988). Note that the empirical estimate is always larger than the limiting theoretical value. This is because band crossing occurs in deformed nuclei and the limiting value (6.10) assumes a spherical system.

   The possibility of negative-energy quasiparticle excitations appears as a general feature of pairing in rotating potentials. In fact, the rotational-alignment effect implies that quasiparticles carry a non-vanishing component Ω_x of angular momentum; thus the excitation of a quasiparticle, for fixed I, is associated with a decrease in the collective rotational energy, corresponding to the last term in (6.9). When the sum of two quasiparticle energies vanishes, one expects a band crossing on the yrast line. For example, in an even–even nucleus, a $v = 2$ band with a large value of $\langle j_1 \rangle + \langle j_2 \rangle$ may cross the $v = 0$ band.

   For nuclei with mass around $A \sim 150$, the first pairs of particles which align are those associated with the $i_{13/2}$ orbital. Making use of standard values of

$\Delta \sim 1.2$ MeV for this mass region, one expects the frequency of the first crossing to be $\hbar\omega \sim 1.2$ MeV/$6 \sim 0.2$ MeV. This rough estimate is consistent with the observed values. The estimate of Garrett *et al.* (1988) given by the equation above for ^{158}Er leads to $\hbar\omega_1 \approx 0.3$ MeV (see Fig. 6.3).

An estimate of the critical angular momentum for total pairing collapse can be obtained making use of Fig. 6.6. Accordingly

$$\frac{\Delta^2}{2d} \approx (E_{\rm rot})_S - (E_{\rm rot})_N \sim \left(\frac{\hbar^2}{2\mathcal{I}_\Delta} - \frac{\hbar^2}{2\mathcal{I}_{\rm rig}}\right) I_{\rm c}^2$$
$$\approx \left(\frac{1}{60} - \frac{1}{120}\right) I_{\rm c}^2 \text{ MeV} \approx \left(I_{\rm c}^2/120\right) \text{ MeV,} \tag{6.11}$$

where the values for the moments of inertia were taken from Fig. 6.3. Note that $\mathcal{I}_{\rm rig}/\hbar^2 \sim 60$ coincides with the value extracted from the analysis of γ–γ correlation (Garrett, Hagemann and Herskind (1986)). Making use of $\Delta \sim 1.2$ MeV and of a standard value $d \sim 0.3 - 0.2$ MeV, one obtains

$$I_{\rm c} \approx 20\hbar. \tag{6.12}$$

Making use of the semiclassical relation $\mathcal{I}\omega_{\rm c} = I_{\rm c}$ (see (6.45)), where $\hbar^2/2\mathcal{I} \approx (1/80)$ MeV, one obtains $\hbar\omega_{\rm c} \approx 0.5$ MeV (see Section 1.9 and Fig. 6.3).

Note that relation (6.11) is equivalent to that used in superconductivity in bulk matter to determine the critical magnetic field.

6.2.2 Pairing in D-states

In Fig. 6.8 the aligned angular momentum i (measured by the difference in angular momentum between the band under consideration and a reference band) of two $i_{13/2}$ neutrons in nuclei around mass 160, is plotted against rotational frequency (approximately half the rotational γ-ray energy) for three bands. The critical frequency is about 0.26 MeV and the aligned angular momentum is $\sim 10\hbar$ ($12\hbar$ is the maximum for two $i_{13/2}$ neutrons). The dashed lines are for two bands in the nucleus ^{163}Yb with one additional neutron located in an orbital labelled either E or F. These orbitals comprise a time-reversed pair at zero rotational frequency and are not very pure shell model states, though their dominant component is $h_{9/2}$. In the even–even nucleus ^{162}Yb, this pair of states (E, F) is available for the pairing correlations, and, in particular, a pair of $i_{13/2}$ neutrons can scatter into it. On the other hand, in ^{163}Yb it is blocked by the odd nucleon for the bands based on either E or F. The pairing correlations are thereby weaker in general, and in particular for a pair of $i_{13/2}$ neutrons. It is easier to unpair and align the $i_{13/2}$ neutrons, and this occurs at a lower rotational frequency, ~ 0.22 MeV, as seen in Fig. 6.8. This shift can be related to the change in the pairing correlations involved and turns out to correspond to a $(20 \div 30)\%$ reduction in pairing. Thus we learn that blocking just one orbital near the Fermi level reduces the pairing correlations
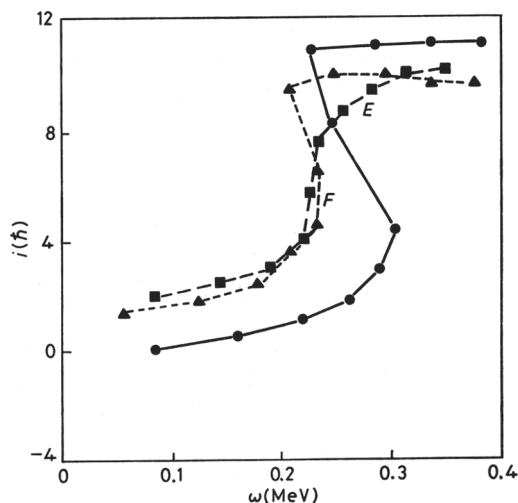
Figure 6.8. The aligned angular momentum, i, is plotted against rotational frequency, ω, for the first backbend ($i_{13/2}$ alignment) region of the lowest-lying (yrast) sequence in ^{162}Yb (continuous line) and for two bands in ^{163}Yb (labelled E and F). The midpoint of the sharp rise is approximately the crossing frequency (after Stephens (1985), Garrett *et al.* (1986)).

appreciably, a result that is confirmed by other kinds of experiments like transfer of pairs of nucleons and directly from the odd–even mass difference. Pairing correlations although playing an extremely important role in the structure of nuclei close to the ground state are weak, and two to three blocked levels of either type (protons or neutrons) are enough to destroy the correlations for that nucleon type.

Conspicuous deviations from the systematic discussed above have been observed (see Fig. 6.9) in specific nuclei. In fact, in ^{161}Er, for example, the crossing of the rotational band based on the [521]3/2$^-$ level shows the effect but not the band based on the [505]11/2$^-$ state. In fact, the $\delta(\hbar\omega)$ associated with the [521]3/2$^-$ orbit is ~ 40 keV, while $\delta(\hbar\omega) \sim 0$ for [505]11/2$^-$.

Both orbitals are close to the Fermi surface at rotational frequency $\omega = 0$. However, the [521]3/2$^-$ orbital has an intrinsic quadrupole moment $q_\nu > 0$, as all the rest of levels in this energy region, while the [505]11/2$^-$ orbital has $q_\nu < 0$ (see Fig. 6.10).

This has important consequences as the nucleus displays quadrupole pairing correlations, aside from monopole pairing correlations. The pairing gap is in this case state dependent (Bes *et al.* (1972), Van Rij and Kahana (1972) and Shimizu *et al.* (1989)), and can be written as (see Section 5.3)

$$\Delta_\nu = G_0 \sum_{\nu'>0} U_{\nu'} V_{\nu'} + G_2 q_\nu \sum_{\nu'>0} U_{\nu'} V_{\nu'} q_{\nu'}. \tag{6.13}$$
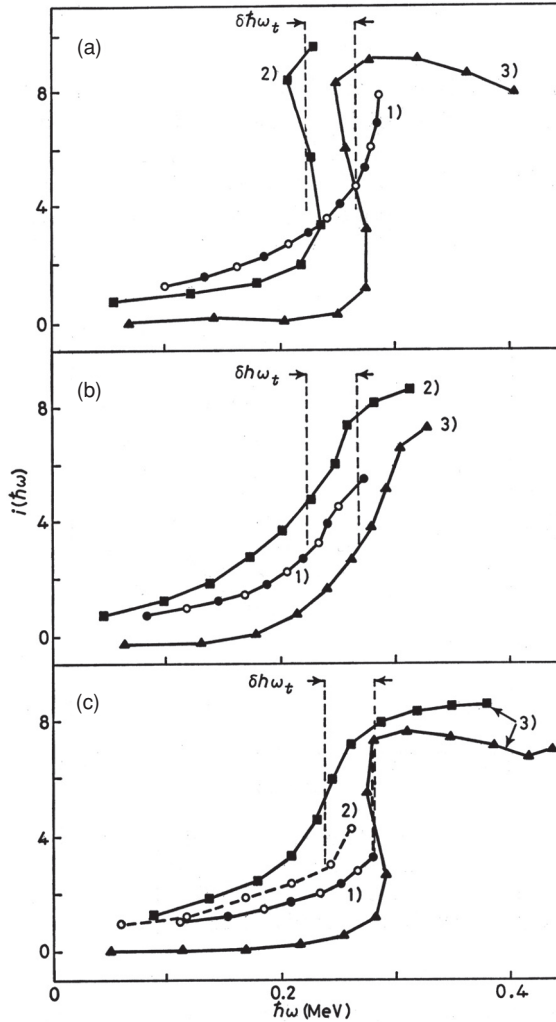
Figure 6.9. Alignment plot for selected decay sequences of rotational states illustrating the observed shifts in crossing frequency: (a) curve 1) ^{181}Os ($7/2^-$[514]), curve 2) ^{181}Os ($7/2^-$[521]), curve 3) ^{182}Os (yrast); (b) curve 1) ^{173}W ($5/2^-$[512]), curve 2) ^{173}W ($1/2^-$[521]), curve 3) ^{172}W (yrast); (c) curve 1) ^{161}Er ($11/2^-$[505]), curve 2) ^{161}Er ($3/2^-$[521]), curve 3) ^{162}Er (yrast). The crossing frequencies are shown by the vertical dashed lines for the ground-state decay sequences in both even- and odd-N isotopes. Signature zero and 1/2 decay sequences are indicated by solid sysmbols, and the $\alpha = -1/2$ sequence is indicated by open symbols. Reprinted from *Physics Letters* B, Vol. 118, Garrett *et al.*, 'Configuration dependent pairing from band crossing frequencies', page 298, Copyright 1982, with permission from Elsevier.

$\lambda(N)$		$\Omega^\pi[Nn_z\Lambda]$	$q_2(\nu)$	$q_4(\nu)$
		$11/2^+[615]$	-3.1	-22.4
$\lambda(115)\rightarrow$		$3/2^-[512]$	-1.2	-18.4
		$1/2^-[510]$	-1.1	-16.7
$\lambda(113)\rightarrow$		$1/2^+[651]$	8.1	78.9
$\lambda(111)\rightarrow$		$7/2^-[503]$	-4.8	31.2
$\lambda(109)\rightarrow$				
$\lambda(107)\rightarrow$				
$\lambda(105)\rightarrow$		$9/2^+[624]$	-0.5	-49.8
		$7/2^-[514]$	-1.7	-25.4
$\lambda(103)\rightarrow$				
$\lambda(101)\rightarrow$		$5/2^-[512]$	-1.5	-37.0
		$1/2^-[521]$	2.9	-16.2
$\lambda(99)\rightarrow$		$7/2^+[633]$	2.0	-49.9
$\lambda(97)\rightarrow$		$5/2^-[523]$	1.3	-35.3
$\lambda(95)\rightarrow$		$5/2^+[642]$	4.1	-29.9
$\lambda(93)\rightarrow$		$3/2^-[521]$	1.8	-30.4
$\lambda(91)\rightarrow$				
$\lambda(89)\rightarrow$		$3/2^+[651]$	5.9	0.8
		$11/2^-[505]$	-5.0	25.4
$\lambda(87)\rightarrow$		$1/2^+[660]$	7.0	28.1
		$3/2^-[532]$	4.2	-6.6
		$1/2^-[530]$	4.9	-1.5
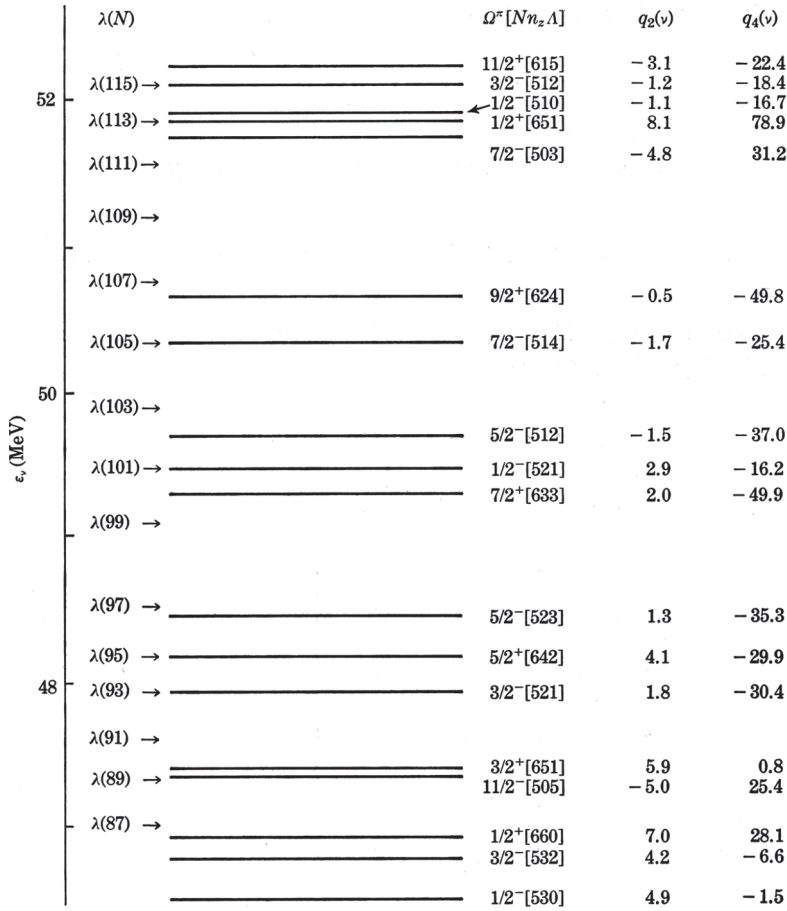
Figure 6.10. Spectrum of neutron Nilsson orbits, identified by the quantum numbers N, n_z and λ (see Nilsson and Ragnarsson (1995)), for rare-earth nuclei calculated assuming $\beta_2 = 0.25$. The position of the Fermi surface, λ, for $\omega = 0.90$ MeV is also indicated for odd neutron numbers. The asymptotic quantum numbers and the quadrupole and hexadecapole moments, $q_2(\nu)$ and $q_4(\nu)$, in units of fm^2 and fm^4, respectively, are indicated for each configuration (from Garrett *et al.* (1982)).

Blocking the orbital ν_b leads to a change in Δ_ν measured by

$$\delta\Delta_\nu(\nu_b) = \Delta_\nu - \Delta_\nu(\nu_b) = GU_{\nu_b}V_{\nu_b}(1 + q_\nu q_{\nu_b}) \approx \frac{G}{2}(1 + q_\nu q_{\nu_b}), \quad (6.14)$$

where we have assumed $U_{\nu_b} \approx V_{\nu_b} \approx 1/\sqrt{2}$ (correct for levels close to the Fermi surface). Making use of the fact that (Nilsson and Ragnarsson (1995))

$$q \sim (3n_z - N)/(N + 3/2),$$

we obtain for the case under discussion

$$
\begin{array}{lll}
[660]\ 1/2^+ & 1.6 \\
[651]\ 3/2^+ & 1.2 \\
[642]\ 5/2^+ & 0.8
\end{array} \Bigg\} \ 1.2,
$$

$$
\begin{array}{lll}
[521]\ 3/2^- & 0.15 \\
[530]\ 1/2^- & 0.6
\end{array} \Bigg\} \ 0.4,
$$

$$
[505]\ 11/2^- \quad -0.8.
$$

Setting $G \approx 27/A$ MeV, one obtains

$$
\delta\Delta_{i_{13/2}}([521]3/2^-) \approx \frac{1}{2}\left(\frac{27}{161}\text{MeV}\right) \times (1 + 1.2 \times 0.4) \approx 130 \text{ keV},
$$

$$
\delta\Delta_{i_{13/2}}([505]11/2^-) \approx \frac{1}{2}\left(\frac{27}{161}\text{MeV}\right) \times (1 - 1.2 \times 0.8) \approx 0 \text{ keV}. \quad (6.15)
$$

This result implies that two particles moving in time-reversal states in the orbital $[505]11/2^-$ do not feel they are in a superfluid nucleus and thus do not contribute to the pairing gap.

The correlation between the shape of a valence quasi-neutron orbital and the shift in band crossing frequencies between neighbouring odd- and even-N isotopes is shown in Fig. 6.11.

6.2.3 Time-reversal violation due to rotation (the $i_{13/2}$ model)

In this subsection we discuss some aspects of the phenomenon of pairing collapse under the influence of strong rotations within a pure $i_{13/2}$ model (Broglia *et al.* (1985a)). We assume the system under study to display axial symmetry around the z-axis, and moreover symmetry with respect to the (x, y)-plane.

The axis of rotation is chosen to be perpendicular to the symmetry axis, which leads to collective rotations. The motion of the particles is controlled by the Nilsson Hamiltonian. The associated single-particle Routhian reads

$$
h_{\text{sp}}^{\omega} = h_{\text{N}}(\varepsilon) - \omega j_x, \quad (6.16)
$$

with

$$
h_{\text{N}}(\varepsilon) = Q j_x^2, \quad (6.17)
$$

where Q is proportional to the quadrupole moment of the system. The Hamiltonian h_{sp}^{ω} is invariant under space reflection (parity) and under rotations through $180°$ about the x-axis, i.e. rotations induced by the operator

$$
R_x = \exp[-i\pi j_x]. \quad (6.18)
$$
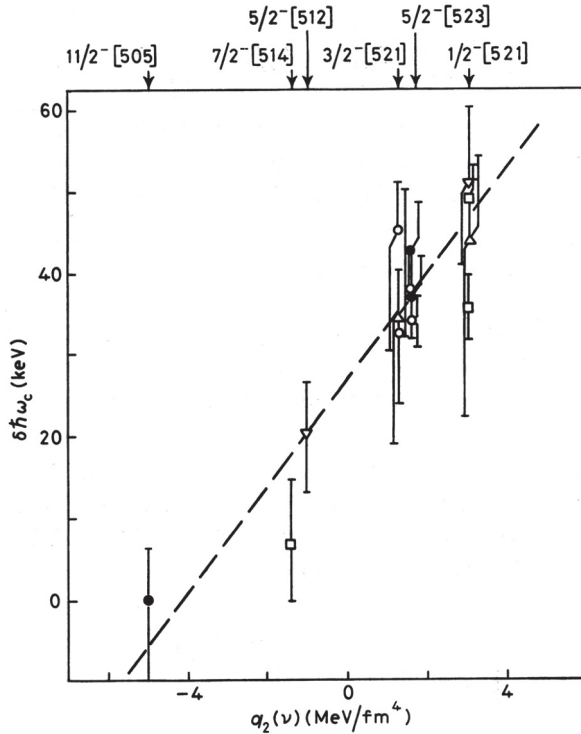
Figure 6.11. Correlation between $\delta\hbar\omega_c$ (see equation (6.15)) and the quadrupole moment, $q_2(\nu)$, of the orbit of the valence quasi-neutron ν: ● Er, ○ Yb, △ Hf, ▽ W, □ Os (see Fig. 6.10). The asymptotic quantum numbers of the various configurations are given at the top of the figure. The dashed line is drawn only to guide the eye. Reprinted from *Nuclear Physics*, Vol. A400, Garrett *et al.*, 'The structure of rotating deformed nuclei,' page 113, Copyright 1982, with permission from Elsevier.

The eigenvalues ε_ν^ω and the eigenstates $|\nu^\omega\rangle$ of the cranking Hamiltonian

$$h_{sp}^\omega|\nu^\omega\rangle = \varepsilon_\nu^\omega|\nu^\omega\rangle \, , \tag{6.19}$$

can thus be labelled by the parity of the state and by the signature quantum number (Bohr and Mottelson (1974)), which is intimately related to the eigenvalues of the operator (6.18).

Let us denote by $|\nu, \Omega_\nu\rangle$ the eigenstates of the Nilsson Hamiltonian $h_N^\omega(\varepsilon)$ and adopt the following phase convention

$$\begin{cases} R_x|\nu, \Omega_\nu\rangle = i(-1)^{\Omega_\nu - 1/2}|\nu, \tilde{\Omega}_\nu\rangle, \\ R_x|\nu, \tilde{\Omega}_\nu\rangle = i(-1)^{\Omega_\nu + 1/2}|\nu, \Omega_\nu\rangle, \end{cases} \tag{6.20}$$

where $|\nu, \tilde{\Omega}_\nu\rangle$ is the time-reversal state to $|\nu, \Omega_\nu\rangle$, while Ω_ν is the magnetic quantum number of the state.

The states

$$|\chi\rangle = \frac{1}{\sqrt{2}}\{(-1)^{\Omega_v+1/2}|v,\Omega_v\rangle + |v,\tilde{\Omega}_v\rangle\} \tag{6.21}$$

and

$$|\tilde{\chi}\rangle = \frac{1}{\sqrt{2}}\{-|v,\Omega_v\rangle + (-1)^{\Omega_v-1/2}|v,\tilde{\Omega}_v\rangle\}, \tag{6.22}$$

which are still related by the time-reversal operation, are eigenstates of R_x with eigenvalues

$$R_x|\chi\rangle = -\mathrm{i}|\chi\rangle \tag{6.23}$$

and

$$R_x|\tilde{\chi}\rangle = \mathrm{i}|\tilde{\chi}\rangle. \tag{6.24}$$

The state (6.21) is said to have signature $\alpha = +\frac{1}{2}$, while the state (6.22) has signature $\alpha = -\frac{1}{2}$.

In the basis $|\chi,\tilde{\chi}\rangle$ the eigenvalue equation (6.19) is block-diagonal, i.e.

$$\begin{pmatrix} h_{\mathrm{N}} - j_x\omega & 0 \\ 0 & h_{\mathrm{N}} + j_x\omega \end{pmatrix} \begin{pmatrix} G \\ H \end{pmatrix} = \varepsilon^\omega \begin{pmatrix} G \\ H \end{pmatrix}. \tag{6.25}$$

The resulting eigenstates can be written as

$$|j\rangle = |\pi,\alpha = \tfrac{1}{2}\rangle = \sum_\chi G_\chi^j |\chi\rangle \tag{6.26}$$

and

$$|\hat{j}\rangle = |\pi,\alpha = -\tfrac{1}{2}\rangle = \sum_\chi H_{\tilde{\chi}}^{\hat{j}} |\tilde{\chi}\rangle. \tag{6.27}$$

Note that the states $|j\rangle$ and $|\hat{j}\rangle$ are related by the operation of time reversal only at $\omega = 0$ (zero rotational frequency). The violation of time-reversal symmetry is measured by the deviation from 1 of the pairing matrix element

$$\langle j\hat{j}'|P^\dagger|0\rangle = \sum_{\chi\chi'} G_\chi^j H_{\chi'}^{\hat{j}'}\langle \chi\chi'|P^\dagger|0\rangle, \tag{6.28}$$

where

$$P^\dagger = \sum_{v_\alpha>0,v_\beta>0} \langle \tilde{v}_\beta|\tau|v_\alpha\rangle a_{v_\alpha}^\dagger a_{\tilde{v}_\beta}^\dagger \tag{6.29}$$

and

$$\langle \chi\chi'|P^\dagger|0\rangle = \langle \chi'|\tau|\chi\rangle = \Delta(\chi',\tilde{\chi}), \tag{6.30}$$
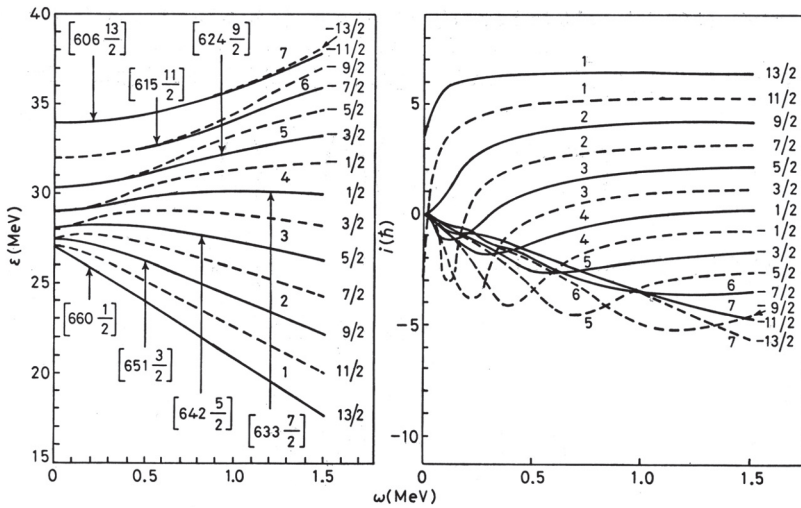
Figure 6.12. Eigenvalues ε_ν^ω and alignments i_ν^ω associated with the eigenstates of the cranked Hamiltonian, for the case of a $1i_{13/2}$ orbital. The eigenvalues are defined through equation (6.25), while the alignment is given by equation (6.32).

the time-reversal operator having been denoted by τ (see Appendix A). Note that the pair field (6.29) coincides with the transfer operator which creates two particles in time-reversal state. From the result (6.30) one obtains

$$M_{j\hat{j}'} = \langle j\hat{j}' | P^\dagger | 0 \rangle = \sum_\chi G_\chi^j H_{\tilde{\chi}}^{\hat{j}}. \tag{6.31}$$

The fact that the pairing field only connects states of different signature can be understood by the fact that at $\omega = 0$, $|j\rangle \to |\chi\rangle$ and $|\hat{j}\rangle \to |\tilde{\chi}\rangle \sim \tau|\chi\rangle$, which are time-reversal states.

In Fig. 6.12 we display the energies ε_ν^ω associated with the diagonalization of $h_{\rm sp}$ in the $i_{13/2}$ single-particle orbital as a function of rotational frequency. In the same figure we also give the alignments

$$i = -\frac{{\rm d}\langle h_{\rm sp}^\omega \rangle}{{\rm d}\omega} = \langle j_x \rangle \tag{6.32}$$

associated with each level.

The square of the pairing matrix elements or pairing overlaps are shown in Fig. 6.13 for a variety of configurations. The most conspicuous features displayed by these quantities can be summarized as follows (see also Broglia (1985c), Nikam and Ring (1987), Nikam *et al*. (1986, 1987), Vigezzi *et al*. (1988)):
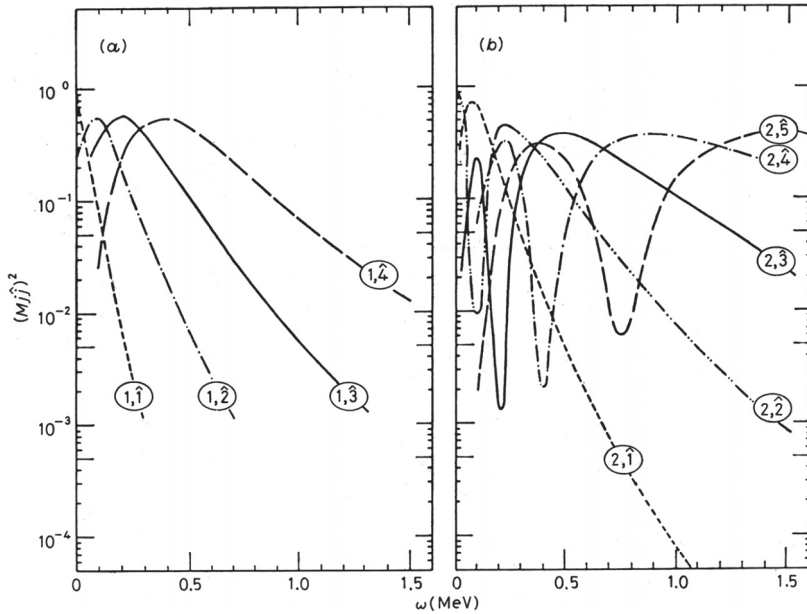
Figure 6.13. Square of the pairing matrix elements as defined in equation (6.31) connecting different eigenstates of the cranking Hamiltonian, as a function of the rotational frequency.

(a) Matrix elements that start being 1 at $\omega = 0$ decrease with increasing values of ω, the opposite being true for those matrix elements which are zero at $\omega = 0$. Many of them become zero again at $\omega \to \infty$ displaying a maximum for finite values of ω.

(b) Aside from the matrix elements $\langle 1, \hat{j} | P_2^\dagger | 0 \rangle$ all other matrix elements oscillate. The first property can be understood making use of the sum rule

$$\sum_{jj'} \langle j \hat{j}' | P^\dagger | 0 \rangle^2 = \Omega, \qquad (6.33)$$

where $\Omega = j + 1/2$ is the number of pairs one can place in the shell, and from the fact that at $\omega = 0$ the twofold degenerate Nilsson states are time-reversal partners, while for $\omega j_x \gg h_N(\varepsilon)$, where m_x is a good quantum number, the time-reversal states are those associated with the values $\pm \Omega_x$ of the magnetic quantum number j_x.

6.2.4 Detailed numerical calculations

In Fig. 6.14 self-consistent calculations (Shimizu *et al.* (1989)) of the BCS neutron pairing gap and of the alignment as a function of the rotational frequency are shown for the nucleus ^{168}Yb.
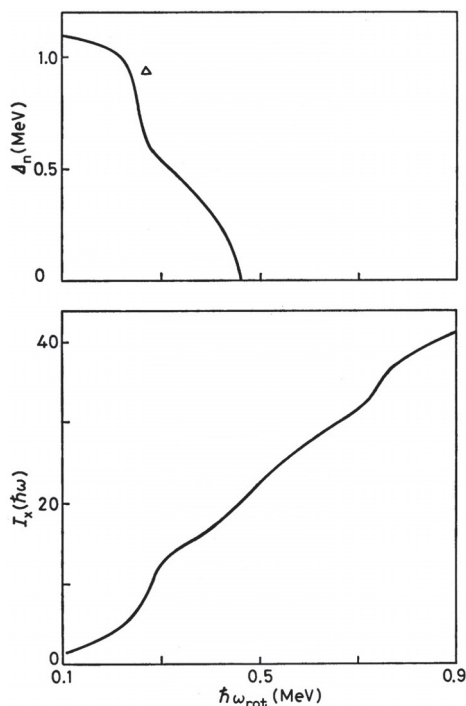
Figure 6.14. The static (BCS) neutron pair gap Δ and the alignment of the lowest $(\pi, \alpha) = (+, 0)$ configuration of $^{168}_{98}$Yb. Reprinted with permission from Shimizu *et al.*, *Rev. Mod. Phys.* **61**:131 (1989). Copyright 1989 by the American Physical Society.

A significant decrease, of the order of 400 keV, is predicted at the frequency of the first crossing ($\sim$0.26 MeV). From here on the pairing gap decreases rather smoothly until, at $\omega_{rot} \sim$0.45 MeV it goes to zero.

A simple estimate of the crossing frequencies and of the critical value ω_c based on equations (6.10) and (6.11) is shown in Table 6.1 and demonstrates overall agreement with the detailed calculations.

From the above discussions and the present results, one can conclude that pairing collapse under the influence of rotation is controlled by the progressive splitting of signature partners and the associated reduction of the pairing matrix elements (time-reversal overlaps). For definite frequencies these overlaps become so small that the corresponding state $(j\,\hat{j}')$ is blocked, and does not contribute to the sum appearing in the BCS equations of the pairing gap. At the frequency where two to three signature pairs are blocked, these equations lead to the trivial solution $\Delta = 0$.

The phenomenon of pairing collapse can be also viewed in terms of the crossing of 2, 4 ... quasiparticle bands with the original ground-state band. This is a

Table 6.1. *Alignments and crossing frequencies for particles moving in a variety of orbitals of ^{168}Yb. The average value $\langle j_x \rangle = ((l + 1/2) + (l - 1/2))/2$ was used to estimate an average crossing frequency through equation (6.10). From the analysis of the irregularities in the $I - \omega$ relation associated with the first band crossing in the rare-earth nuclei ($i_{13/2}$ alignment), it is found that the alignment is less ($\sim 25\%$) than the maximun value $i = j = 13/2$. The particle retains a strong coupling to the symmetry axis, and it is only the component of angular momentum along this symmetry axis that can easily be aligned. The quantity $\overline{j_x} = \langle j_x \rangle - 25\%$ was used to obtain somewhat more realistic estimates $\overline{\omega_1}$ of the crossing frequencies (see discussion following equation (6.10)).*

	$\langle j_x \rangle (\hbar)$	$\langle \omega_1 \rangle (MeV)$	$\overline{j_x}(\hbar)$	$\overline{\omega_1}(MeV)$
i	6	0.20	4.5	0.27
h	5	0.24	3.8	0.32
g	4	0.30	3.0	0.40
f	3	0.40	2.3	0.50

valid interpretation to the extent that one does not require that all bands have a strict existence at all rotational frequencies. In fact, in the case under discussion only the first crossing is clearly seen experimentally.

6.3 Pairing fluctuations

For rotational frequencies ω smaller than the critical frequency ω_c, where the BCS gap becomes zero, the pairing contribution to the ground-state energy is proportional to the square of the number of particles. That is, $E_0 \sim GN^2$, typical of a pairing rotational band (see Chapters 4 and 5). The contribution to E_0 of the zero-point fluctuations associated with the pairing modes is $E_{gsc} \sim GN$, leading to a ratio $r \sim E_{gsc}/E_0 \sim N^{-1}$. For rotational frequencies $\omega > \omega_c$, that is for normal systems, $E_{gsc} \sim GN$ as before, while $E_0 \sim GN$ typical of pairing vibrational bands. The ratio r is in this case of order 1. It is thus expected that the effects of zero-point fluctuations associated with pairing vibrations will be much more important at rotational frequencies $\omega \gtrsim \omega_c$ than at $\omega < \omega_c$.

In the present subsection we study some of the consequences these fluctuations have on a variety of properties of strongly rotating nuclei. We carry out our investigations for high rotational frequencies $\omega > \omega_c$, i.e. for normal systems. The calculations are done in the framework of the cranked shell model treating the

pairing vibrations of the normal system in the RPA. By decreasing ω, but keeping it always larger than ω_c, we gradually approach the pairing phase transition. That is, we study the onset of the normal to superfluid phase transition at zero temperature, taking into account the fluctuations induced by pairing vibrations (see Barranco *et al.* (1987)).

The equations determining the properties of pairing vibrations in normal systems, i.e. in systems with fixed number of particles, are, in the random-phase approximation (Broglia *et al.* (1986), Shimizu *et al.* (1989)),

$$\sum_n(\beta = +2) = \frac{1}{G}, \tag{6.34}$$

$$\sum_n(\beta = +2) = \sum_{kk'} \frac{M_{k\hat{k}'}^2 U_k^2 U_{\hat{k}'}^2}{e_k + e_{\hat{k}'} - W_{+2}(n)} + \sum_{i\hat{i}'} \frac{M_{i\hat{i}'}^2 U_i^2 U_{\hat{i}'}^2}{e_i + e_{\hat{i}'} + W_{+2}(n)} \tag{6.35}$$

and

$$\sum_{kk'} X_{k\hat{k}'}^2(+2, n) - \sum_{ii'} Y_{i\hat{i}'}^2(+2, n) = 1. \tag{6.36}$$

The amplitudes X and Y are defined as

$$
\begin{cases}
X_{k\hat{k}'}(+2, n) = \dfrac{\Lambda_{+2}(n)M_{k\hat{k}'}U_k^2 U_{\hat{k}'}^2}{e_k + e_{\hat{k}'} - W_{+2}(n)}, \\[4mm]
Y_{i\hat{i}'}(+2, n) = \dfrac{\Lambda_{+2}(n)M_{i\hat{i}'}U_i^2 U_{\hat{i}'}^2}{e_i + e_{\hat{i}'} + W_{+2}(n)},
\end{cases}
\tag{6.37}
$$

the quantity $\Lambda_{+2}(n)$ being the particle-vibration coupling strength determined from the normalization condition (6.36). The quantities $M_{i\hat{i}'}$ are the pairing matrix elements connecting states with different signatures, while e_i and $e_{\hat{i}'}$ are the associated single-particle energies measured from the Fermi energy. The pairing vibrations are labelled by the transfer quantum number $\beta = \pm 2$. The quantities U^2 and V^2 are either 1 or 0 according to the occupancy of the state. The equations above thus describe the pair addition modes, i.e. vibrations which increase the number of particles by 2. The index n indicates whether the solution of equation (6.35) one considers corresponds to the state with lowest energy ($n = 1$), next to lowest ($n = 2$), etc.

Similar equations describe the pair removal modes, i.e. vibrations which diminish the number of particles by two units. It is noted that all quantities in equation (6.35), with the exception of the pairing coupling constant G, depend on the rotational frequency ω. This is, of course, an oversimplification of the problem, in view of the fact that a non-negligible contribution to G arises from the exchange of collective vibrations between pairs of nucleons forming Cooper pairs (see Chapters 8–10).

The Mottelson–Valatin (1960) critical rotational frequency for which the BCS equations have a solution $\Delta = 0$ coincides with the frequency for which the energy of the pair-addition and pair-removal modes of the normal system goes to zero, i.e.

$$(W_{+2}(n))_{\omega_c} = (W_{-2}(n))_{\omega_c} = 0. \qquad (6.38)$$

In fact, in this case equation (6.35) is equivalent to the BCS gap equation if one interprets the energies e_j as quasiparticle energies.

The influence of pairing fluctuations on different nuclear properties can be calculated in the RPA. In particular, the contribution to the energy of a given configuration of parity π and signature α is given by (see Section 8.4)

$$E_{\text{gsc}}(\pi, \alpha) = \frac{1}{2} \sum_{\beta = \pm 2, n} W_\beta(\pi\alpha; n) - \frac{1}{2} \sum_{jj'}(e_j + e_{\hat{j}'}), \qquad (6.39)$$

which is the sum of the energies of the pair-addition and subtraction modes measured from the energy of the unperturbed two-particle poles ($e_j + e_{\hat{j}}$). With j we indicate both levels above ($j > k$) and below ($j < i$) the Fermi energy. The quantity E_{gsc} is thus equal to the sum of the correlation energies of all pair-addition and pair-subtraction modes.

The total energy of the variety of configurations calculated in the rotating frame ('Routhian') is

$$e(\pi, \alpha) = \langle h_{\text{sp}}^\omega \rangle + E_{\text{gsc}}. \qquad (6.40)$$

The average angular momentum associated with these configurations along the axis of rotation can be written as

$$i_x(\pi, \alpha) = -\frac{\partial e(\pi, \alpha)}{\partial \omega} = \langle j_c \rangle - \frac{\partial E_{\text{gsc}}}{\partial \omega}. \qquad (6.41)$$

Examples of the quantities, again for ^{168}Yb, are shown in Fig. 6.15. The bands have different parity signature quantum numbers (π, α).

The ease with which the $(+, 0)$ configuration reacts to pairing correlations, leading to smaller alignments, reflects the fact that in this configuration the lowest levels of both even and odd parity are filled with an even number of particles. Consequently the configuration $(+, 0)$ is the analogue to the BCS vacuum at $\omega > \omega_c$.

The configuration $(-, 0)$ or $(-, 1)$ is associated with situations where one has an odd number of particles in both even- and odd-parity levels. They thus correspond to two-quasiparticle configurations at $\omega < \omega_c$, relative to the $(+, 0)$ configuration. This implies that the $(-, 0)$ and $(-, 1)$ configurations are affected by a high degree of blocking. Consequently, pairing vibrations typical of normal systems can develop at a lower frequency than in the case of the $(+, 0)$ configurations. That is, one needs only moderate values of ω to achieve the situation in which the fluctuations of the pairing gap are as large as its average value.
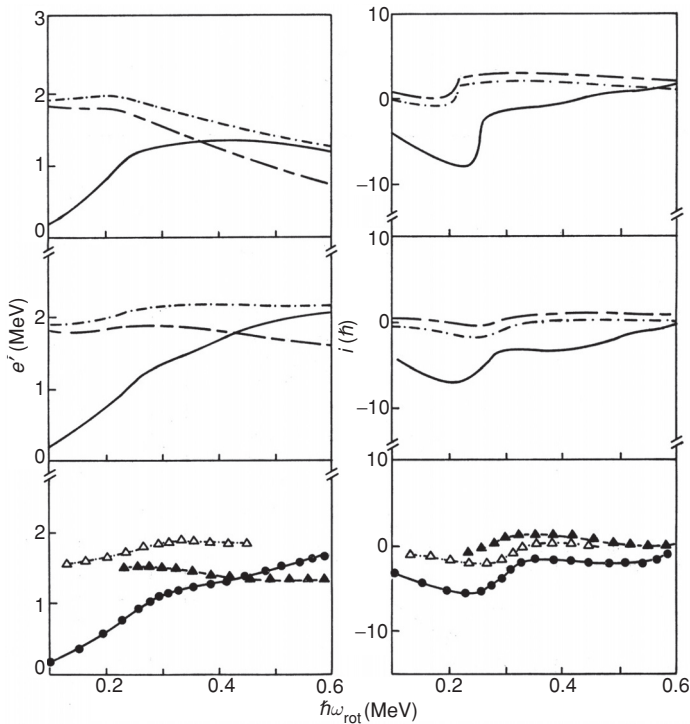
Figure 6.15. Comparison of calculated Routhians, with fluctuations (middle portion) and without fluctuations (top portion), and experimental Routhians (bottom portion), e' (left-hand side), and alignments, i (right-hand side), for various configurations in $^{168}_{92}$Yb. The $(+, 0)$ configuration is denoted by solid lines and solid dots, $(-, 0)$ by dot-dashed lines and open triangles and $(-, 1)$ by double-dashed lines and solid triangles. The calculated and experimental values are referred to reference configurations with constant moment of inertia of $62\hbar^2\,\text{MeV}^{-3}$ and $66\hbar^2\,\text{MeV}^{-1}$, respectively. Reprinted with permission from Shimizu *et al.*, *Rev. Mod. Phys.* 61:131 (1989). Copyright 1989 by the American Physical Society.

6.4 Moments of inertia

As a consequence of the interplay between collective and single-particle motions, there are a variety of moments of inertia one can measure and compare with detailed calculations (Broglia *et al.* (1985b), Szymanski (1985)). The first distinction to be made is between kinematic and dynamic values (Bohr and Mottelson (1974)).

The moment of inertia defined as the first derivative of the rotational energy with respect to spin

$$\frac{\mathcal{I}^{(1)}}{\hbar^2} = I \left(\frac{\mathrm{d}E}{\mathrm{d}I}\right)^{-1} = \frac{I}{\hbar\omega} \tag{6.42}$$

is the so-called 'kinematic' moment of inertia, because it has to do with the motion of the system, the ratio of angular momentum to angular frequency. It is

also apparent that the second derivative leads to the definition

$$\frac{\mathcal{I}^{(2)}}{\hbar^2} = \left(\frac{d^2 E}{dI^2}\right)^{-1} = \frac{dI}{d(\hbar\omega)}, \tag{6.43}$$

where $\mathcal{I}^{(2)}$ is called the 'dynamic' moment of inertia, because it has to do with the way the system will respond to a force.

In general $\mathcal{I}^{(1)}$ and $\mathcal{I}^{(2)}$ are different in rotating nuclei, because of the effect of the Coriolis term $\sim I \cdot j$.

A simple approximation for the rotational energy is

$$E(I) = E_0 + \frac{(I - i_0)^2}{2\mathcal{I}}, \tag{6.44}$$

where $\mathcal{I}$ is identified as the second moment of inertia. The quantity i_0 is related in some general way to the part of angular momentum carried out by the single-particle motion. It should not, however, be confused with the actual particle alignment, as can be seen from Fig. 6.16.
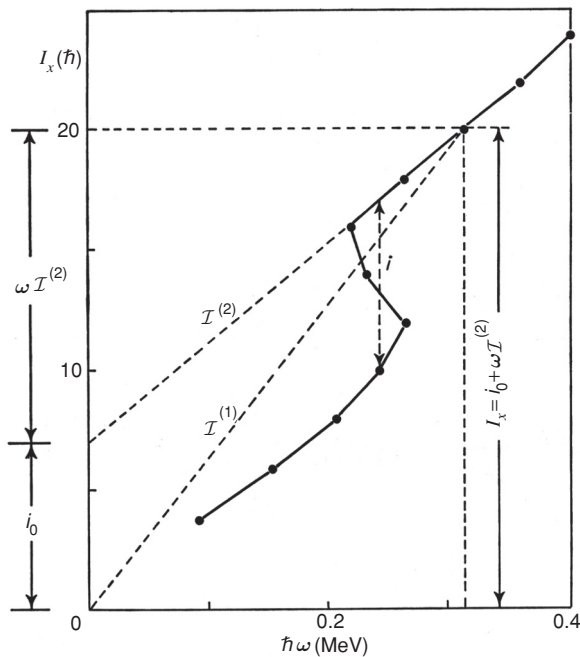
Figure 6.16. Illustration of apparent alignment i_0. Apparent alignment (i_0), the $\omega = 0$ intercept of an extrapolation of the local dynamic moment of inertia, $\mathcal{I}^{(2)}$, can be defined as the difference between the kinematic, $\mathcal{I}^{(1)}$, and dynamic moments of inertia. The various quantities entering this definition are indicated in the figure. The $I_x(\omega)$ data are for the ground-state, $(-, 1/2)$ configuration of $^{159}_{91}$Er. Reprinted with permission from Shimizu *et al.*, *Rev. Mod. Phys.* 61:131 (1989). Copyright 1989 by the American Physical Society.
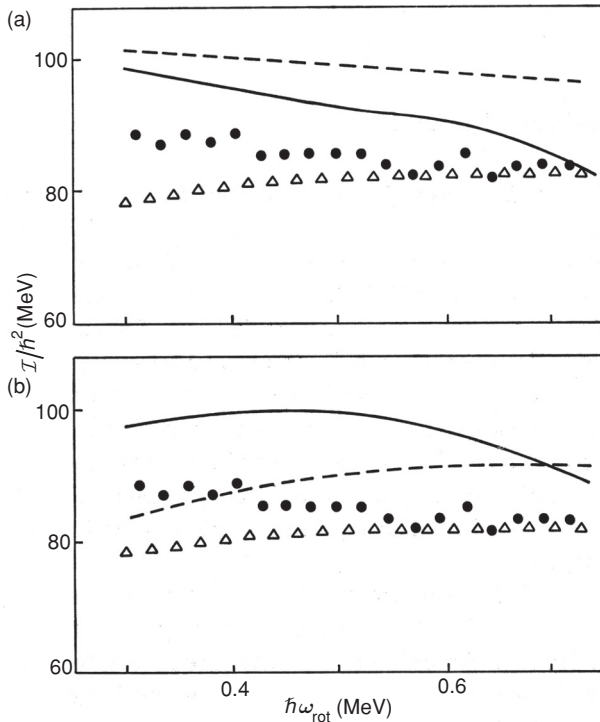
Figure 6.17. The kinematic and the dynamic moment of inertia, $\mathcal{I}^{(1)}$ and $\mathcal{I}^{(2)}$, associated with the superdeformed band of ^{152}Dy (see Fig. 6.18) as functions of the rotational frequency (for a quadrupole deformation parameter) ($\varepsilon_2 = 0.58$): (a) results without taking into account pairing fluctuations, (b) results including pairing fluctuations: theory: $-\mathcal{I}^{(2)}$, $---\mathcal{I}^{(1)}$; experiment: $\bullet\bullet\bullet \mathcal{I}^{(2)}$, $\triangle\triangle\triangle \mathcal{I}^{(1)}$. The absolute value of $\mathcal{I}$ is overestimated because the Strutinsky renormalization of the angular momentum was left out. Reprinted from *Physics Letters* B, Vol. 198, Shimizu *et al.*, 'Role of static and dynamic pairing correlations in the superdeformed band of ^{152}Dy, page 35, Copyright 1987, with permission from Elsevier.

The parametrization (6.44) arises from the cranking model where the canonical frequency ω, which determines the magnitude of the rotational perturbation, is approximately given by

$$\omega = \frac{1}{\mathcal{I}_0}(I - i_0) \sim \frac{R}{\mathcal{I}_0}, \tag{6.45}$$

where R is the angular momentum of the collective rotation and $\mathcal{I}_0$ the moment of inertia of the rotor in the particle-rotor model.

Examples of the role played by pairing fluctuations in the behaviour of $\mathcal{I}^{(1)}$ and $\mathcal{I}^{(2)}$ with rotational frequency are shown in Fig. 6.17 for the case of the superdeformed band of ^{152}Dy.

6.5 Condensation-induced tunnelling

The interplay between collective degrees of freedom and single-particle motion common to all many-body systems is encountered in the study of nuclear structure in a particular concrete form. This is because of the possibility of detailed studies of individual quantum states, as carried out, for example, in the case of the nuclear potential energy considered as a function of the shape. While the general features of this 'potential-energy function' can be described in terms of bulk properties of the nuclear matter such as surface tension and electrostatic energy, the specific geometry of the quantized orbits of the individual nucleons contributes important anisotropic effects; a striking consequence is the occurrence of nuclear-equilibrium shapes deviating strongly from spherical symmetry.

The effect of the shell structure on the nuclear potential energy has come into perspective in the study of superdeformed bands, the first one observed (see e.g. Nolan and Twin (1988)) being that of the nucleus ^{152}Dy (see Fig. 6.18, see also Åberg (1987)). Superdeformed states are associated with quadrupole deformed nuclear shapes, where the ratio between the larger and the smaller
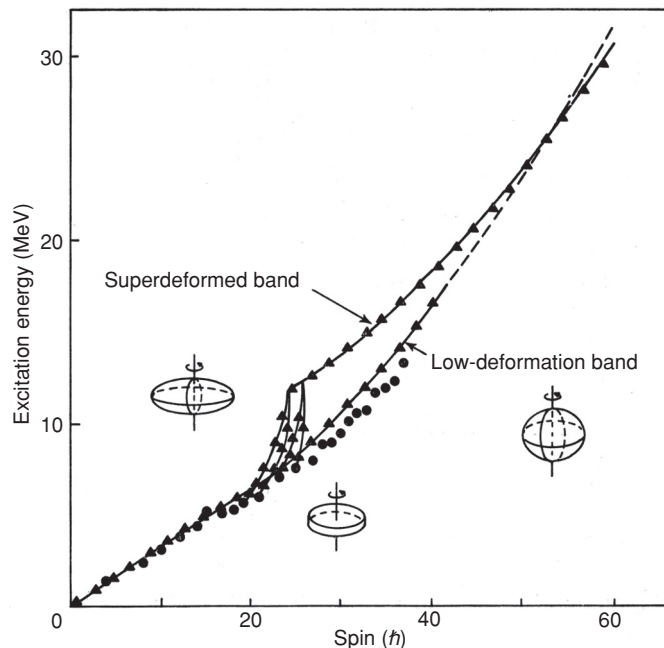
Figure 6.18. The experimental knowledge about ^{152}Dy includes states at three different deformations: non-collective oblate states, a collective low-deformation band (presumably prolate) and a collective superdeformed band. Some typical decay paths de-exciting the superdeformed band to oblate states are illustrated (dots). Reprinted, with permission, from the *Annual Review of Nuclear Science*, Volume 23 © 1973 by Annual Reviews www.annualreviews.org

radii is $2:1$. This is probably the largest deformation a nucleus can hold without fissioning, hence the name. The microscopic basis for the appearance of superdeformed configurations reflects a special stability associated with the shell structure, and is intimately connected with that found for the existence of fission isomers (Michaudon (1973)).

The nature of these shells can be understood in a simple manner by reference to one-particle motion in a spheroidal deformed harmonic-oscillator potential. As illustrated in Fig. 6.19, the degeneracies of the isotropic oscillator are removed by the deformation, but new major shells (degeneracies) reappear when the oscillator frequencies in the different directions have rational ratios.

Especially large effects occur for a deformation with the frequency ratio $\omega_\perp : \omega_3 = 2:1$, and the associated nucleon numbers for closed shells are $N = 80, 110, 140, \ldots$. The nuclear potential differs from the harmonic oscillator in the radial dependence and in the occurrence of a large spin-orbit coupling. The inclusion of these effects leaves intact the main features of the oscillator shell structure in the $2:1$ potential, but modifies the closed-shell numbers to $N = \ldots, 86, 116, \ldots$ (Bohr and Mottelson (1973)).

Once the superdeformed yrast band of ^{152}Dy is populated with a spin $I \sim 60\hbar$, the nucleus remains in it through eighteen collective $E2$ transitions (Twin *et al.* (1986)) until suddenly at spin $I = 24\hbar$ and about 5 MeV above the yrast line it terminates within an angular interval $\Delta I \sim (2 \div 4)\hbar$. This observation requires that a mechanism be identified which within a narrow range of $2 \div 4$ units of $\hbar$ can change the tunnelling probability between the superdeformed and the normal minimum by about six orders of magnitude.

Although the barrier between the superdeformed and the normal minima changes with spin, all calculations predict a smooth variation of it (Ragnarsson and Åberg (1986)) (see Fig. 6.20).

The sudden transition out of the superdeformed minimum at spin $I = 24\hbar$ is likely to be related to the onset of pairing caused by the disalignment of the lowest pair of $j_{15/2}$ quasiparticles, taking place at frequency ~ 0.3 MeV (Shimizu *et al.* (1987)) (see Section 6.2), although other mechanisms may play a role (see, e.g. Åberg (1999), Andreoiu *et al.* (2003), Sergeant *et al.* (2002)). This change in the pairing gap strongly reduces the inertial parameter D (see equations (7.6) and (7.8)), leading to a large increase of the tunnelling probability, as shown in Fig. 6.21. It is likely that these results are the clearest indication to date of a pairing collapse taking place in nuclei as a function of the angular momenta. The discussion of this subject is continued in Chapter 7.

6.6 Response function technique to calculate RPA fluctuations

In the present section we shall study the behaviour of the pairing correlation energy, and of the pairing gap of a superfluid, for deformed strongly rotating
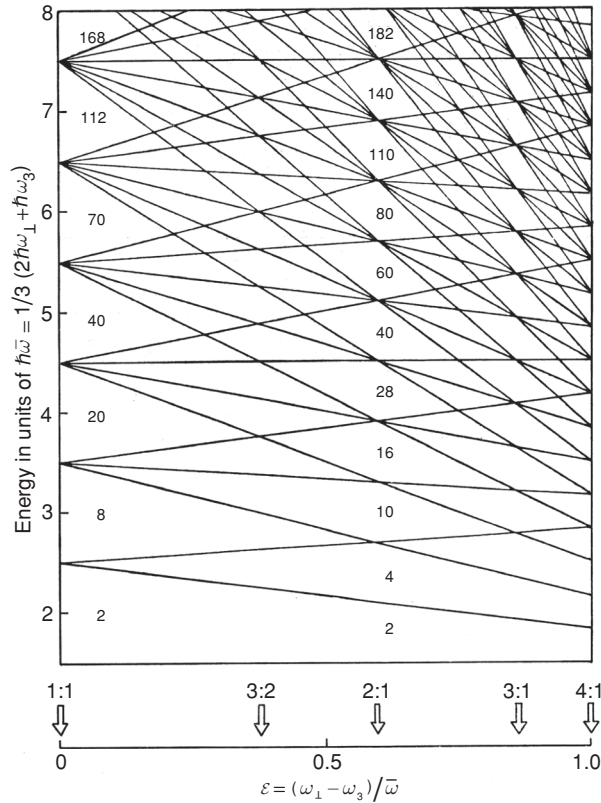
Figure 6.19. Shell structure in anisotropic harmonic-oscillator potential. This figure shows the single-particle energy levels, as a function of deformation, in a prolate axially symmetric oscillator potential. $V = (1/2)M(\omega_\perp^2(x_1^2 + x_2^2) + \omega_3^2 x_3^2)$, $E = \hbar\omega_\perp(n_\perp + 1) + \hbar\omega_3(n_3 + 1/2)$. The frequencies ω_3 and $\omega_\perp$ refer to motion parallel and perpendicular to the symmetry axis, while $\bar{\omega}$ is the mean frequency. The single-particle states can be specified by the number of quanta n_3 and $n_\perp$, and each energy level has a degeneracy $2(n_\perp + 1)$, due to the spin and the degeneracy in the motion perpendicular to the axis. Additional degeneracies leading to the formation of major shells may occur when the ratio of the frequencies $\omega_\perp : \omega_3$ is equal to the ratio between integers. The deformations corresponding to the most prominent shell structure effects are indicated by the arrows labelled by the corresponding frequency ratio. For the shells with frequency ratio 1 : 1 (spherical shape) and 2 : 1, the figure gives the particle numbers for closed-shell configurations (from Bohr and Mottelson (1973)). Reprinted, with permission, from the *Annual Review of Nuclear Science*, Volume 23 © 1973 by Annual Reviews www.annualreviews.org

nuclei as a function of the rotational frequency, taking into account pairing fluctuations in the RPA.

In the quasiparticle basis, the correlation energy takes the form

$$E_{\text{corr}}^{\text{RPA}} = \frac{1}{2}\left[\sum_n \omega_n - \sum_{\alpha<\beta} E_{\alpha\beta}\right], \tag{6.46}$$
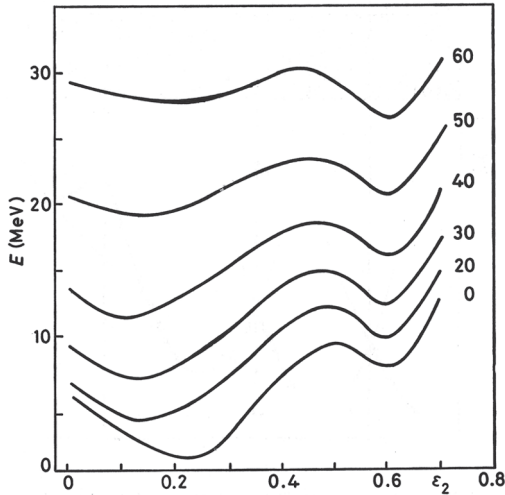
Figure 6.20. Potential energy of ^{152}Dy as a function of deformation parameter ε_2 for different values of the angular momentum.

where ω_n are the RPA eigenfrequencies, $E_{\alpha\beta} \equiv E_\alpha + E_\beta$ being the unperturbed two-quasiparticle energies. Because the different RPA modes contribute democratically to $E_{\text{corr}}^{\text{RPA}}$, to calculate this quantity one needs to determine very many, closely spaced, RPA eigenmodes. This is particularly true in the case where symmetries of the mean field are spontaneously broken, such as in the case of superfluid and deformed nuclei, where the detailed computation of the contribution of every single RPA root to $E_{\text{corr}}^{\text{RPA}}$ becomes unfeasible. To avoid this problem, Shimizu *et al.* (1989) developed a method to calculate the correlation energy, making use of response function techniques, and applied it to the study of pairing correlations in rapidly rotating nuclei. The essence of the method consists in expressing the RPA correlation as an integral in terms of the RPA response function, which can be calculated without explicitly solving the RPA eigenvalue problem. These techniques have been extended to deal with the Anderson–Goldstone–Nambu modes (Donati *et al.* (1999a)), and to calculate the nucleon effective mass in superfluid, deformed, rotating nuclei (Donati *et al.* (1999b)). An equivalent method was developed by Dönau *et al.* (1999).

Following Shimizu *et al.* (2000), we start from the Hamiltonian,

$$H = H_0 + V, \qquad (6.47)$$

where H_0 is the unperturbed one-body (mean-field) Hamiltonian and V is the residual two-body interaction, which is assumed to be of multi-separable form,

$$V = -\frac{1}{2} \sum_\rho \chi_\rho Q_\rho Q_\rho, \qquad (6.48)$$
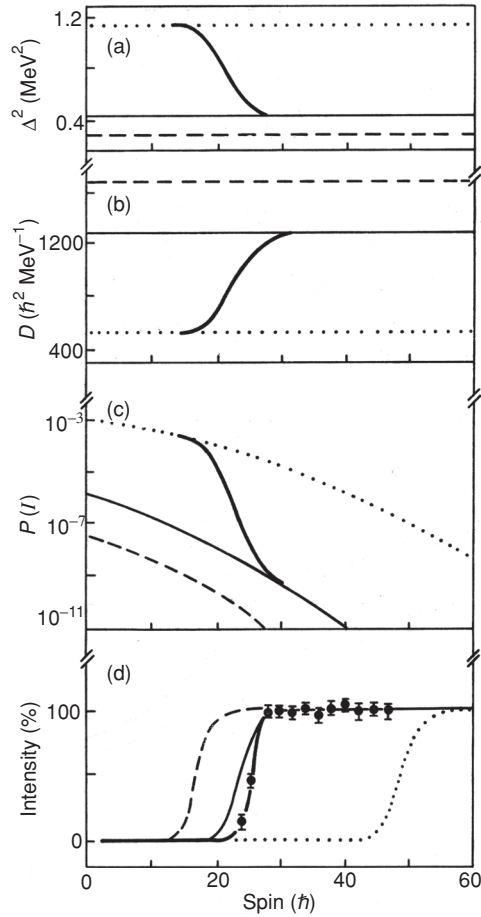
Figure 6.21. Four different possibilities for the variation of the square of the pairing gap with angular momentum are considered. (a) illustrates its influence on the barrier penetrability. Shown in graphs (b) and (c) is the associated variation of the inertial-mass parameter D and the penetrability factor $P(I)$. In (d) the relative intensity of the superdeformed band is shown as a function of the angular momentum in comparison with the experimental datum in comparison with the experimental data. Reprinted with permission from Herskind *et al.*, *Phys. Rev. Lett.* **59**: 2416–19 (1988). Copyright 1988 by the American Physical Society.

with Q_ρ being a one-body Hermitian operator while χ_ρ is the strength of the interaction in channel ρ. The associated ground-state energies and state vectors of H_0 and H are denoted E_0, $|\Phi_0\rangle$ and E, $|\Psi\rangle$, respectively. Turning on the interaction adiabatically, the correlation energy can be written as (Fetter and Walecka (1971))

$$E_{\text{corr}} \equiv E - E_0 = \int_0^1 \mathrm{d}\lambda \, \langle \Psi(\lambda)|V|\Psi(\lambda)\rangle. \tag{6.49}$$

In this equation $|\Psi(\lambda)\rangle$ is the ground state of the λ-scaled Hamiltonian $H(\lambda) \equiv H_0 + \lambda V$. Within the RPA approximation, the above expression can be rewritten by making use of a contour integration as

$$
\begin{aligned}
E_{\text{corr}}^{\text{RPA}} &= -\frac{1}{2} \int_0^1 d\lambda \sum_{\rho,n} \chi_\rho \mathcal{Q}_{\rho,n}^{(\lambda)*} \mathcal{Q}_{\rho,n}^{(\lambda)} \\
&= -\frac{1}{4\pi i} \int_0^1 d\lambda \oint_C dz \sum_\rho \left[\mathcal{R}_{\rho\rho}^{(\lambda)}(z) \chi_\rho \right],
\end{aligned}
\tag{6.50}
$$

in terms of the λ-scaled RPA response function (matrix),

$$
\mathcal{R}_{\rho\sigma}^{(\lambda)}(\omega) \equiv \sum_n \left[\frac{\mathcal{Q}_{\rho,n}^{(\lambda)*} \mathcal{Q}_{\sigma,n}^{(\lambda)}}{\omega_n^{(\lambda)} - \omega} + \frac{\mathcal{Q}_{\rho,n}^{(\lambda)} \mathcal{Q}_{\sigma,n}^{(\lambda)*}}{\omega_n^{(\lambda)} + \omega} \right],
\tag{6.51}
$$

where $\mathcal{Q}_{\rho,n}^{(\lambda)} = \langle n(\lambda)| Q_\rho |\Psi(\lambda)\rangle_{\text{RPA}}$, and the contour C encloses all the positive λ-scaled RPA eigenvalues $z = \omega_n^{(\lambda)}$ clockwise. Note that $\mathcal{R}_{\rho\sigma}^{(\lambda)}(\omega)$ can be calculated as

$$
\mathcal{R}^{(\lambda)}(\omega) = \left[1 - R(\omega) \chi \lambda \right]^{-1} R(\omega),
\tag{6.52}
$$

in terms of $\chi = (\Delta_{\rho\sigma} \chi_\rho)$ and the unperturbed response function (matrix), $R_{\rho\sigma}(\omega)$, which is defined by replacing $\mathcal{Q}_{\rho,n}^{(\lambda)}$ and $\omega_n^{(\lambda)}$ in equation (6.51) with unperturbed quantities, $q_{\rho,\alpha\beta} = \langle \alpha\beta | Q_\rho | 0 \rangle$ and $E_{\alpha\beta}$.

By choosing a common contour C for all values of $0 < \lambda < 1$, one may exchange the order of integration in equation (6.50) (Pines (1963), Appendix C). The selected path is the one shown in Fig. 6.22 passing through the origin of the complex z-plane in keeping with the presence of (non-normalizable) zero-energy modes (the symmetry-recovering or Anderson–Goldstone–Nambu modes, Chapter 4) in the RPA spectrum ($\omega_{n=\text{AGN}} \to 0$ as $\lambda \to 1$). In this case the λ-integration in equation (6.50) converges because $|\mathcal{Q}_{\rho,n=\text{AGN}}^{(\lambda)}|^2 \sim 1/\sqrt{1-\lambda}$ as $\lambda \to 1$. After performing the λ-integration analytically, one obtains

$$
E_{\text{corr}}^{\text{RPA}} = \frac{1}{4\pi i} \oint_{C_{1a}} F(z) dz,
\tag{6.53}
$$
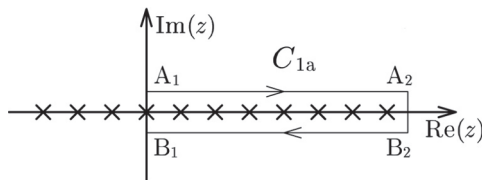
Figure 6.22. An illustration of the integration contour in the complex z-plane used in equation (6.53). Crosses denote the positions of all the λ-scaled RPA roots for arbitrary values of $0 < \lambda < 1$, i.e. $\text{Re}(A_2) = \text{Re}(B_2) > \max_{n,\lambda}\{\omega_n^{(\lambda)}\}$.

where

$$F(z) \equiv -\int_0^1 \mathrm{Tr}\Big[\mathcal{R}^{(\lambda)}(z)\chi\Big]\mathrm{d}\lambda = \log\big(\det\big[1 - R(z)\chi\big]\big). \qquad (6.54)$$

Rewriting the determinant as a function of the RPA and unperturbed energies, one obtains

$$F(z) = \sum_n \Big[\log(z - \omega_n) + \log(z + \omega_n)\Big]$$
$$- \sum_{\alpha < \beta} \Big[\log(z - E_{\alpha\beta}) + \log(z + E_{\alpha\beta})\Big]. \qquad (6.55)$$

Thus, equation (6.53) is the sum of integrals of the complex multi-valued logarithmic functions of type $\log(z - p)$, where the real value p (in our case ω_n or $E_{\alpha\beta}$) indicates a branch point. Here the principal branch of the logarithmic function should be taken in accordance with the choice of path C_{1a}, i.e. $-\pi < \arg\log(z - p) \leq \pi$, and the segment of the real axis with $z < p$ is the branch-cut. One can now integrate equation (6.53) around all the branch points within C_{1a} by deforming the path and using for each of them a clockwise circular path C_p centred at the point itself, i.e.

$$\int_{C_p} \log(z - p)\,\mathrm{d}z = 2\pi\mathrm{i}\,R_p, \qquad (6.56)$$

where R_p is the radius of the circle C_p. Considering that R_p is ω_n or $E_{\alpha\beta}$, it can be shown that equation (6.53) leads to the original expression given in equation (6.46). The contribution associated with the zero mode vanishes in keeping with the fact that in this case the path of integration becomes a semicircle. This can also be seen by direct evaluation of the integral in equation (6.56) in the case where C_p is a semicircle centred at zero with $R_{p=0} \to 0$.

Making use of a limiting procedure and the following properties of the function $F(z)$,

$$[F(z)]^* = F(-z^*), \quad F(-z) = F(z), \qquad (6.57)$$
$$F(z) \to o(1/z^2) \quad \text{as} \quad |z| \to \infty, \qquad (6.58)$$

it can be shown that equation (6.53) can be written as

$$E_{\mathrm{corr}}^{\mathrm{RPA}} = \frac{1}{2\pi} \lim_{\varepsilon \to 0+} \int_0^\infty \mathrm{Im}\big[F(\omega + \mathrm{i}\varepsilon)\big]\mathrm{d}\omega, \qquad (6.59)$$

which is the formula utilized in (Shimizu *et al.* (1989)). To obtain this result one deforms the path shown in Fig. 6.22 taking the part A_2 and B_2 to infinity and A_1B_1 infinitely close to the origin ($\varepsilon \to 0$). In this case the contributions from segments A_2B_2 and A_1B_1 vanish, those arising from A_1A_2 and B_1B_2 being equal.
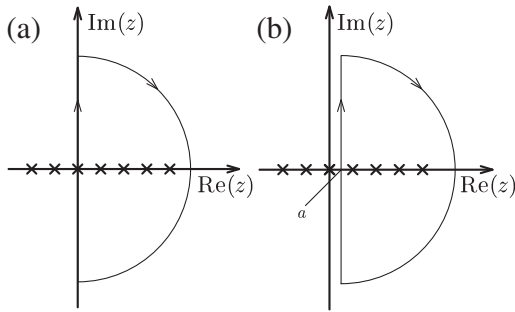
Figure 6.23. Modified integration contour from Fig. 6.22 found to be more suitable to calculate the RPA correlation energy. Taking the limit of infinite radius of the semicircle, the corresponding contribution vanishes.

In order to present a more efficient way to evaluate the RPA correlation energy, the integration path in Fig. 6.22 is modified to the one shown in Fig. 6.23a. Then the contribution from the semicircle vanishes as its radius goes to infinity because of the asymptotic property given in equation (6.58). Using also the properties given in equation (6.57), we obtain

$$E_{\text{corr}}^{\text{RPA}} = \frac{1}{2\pi} \int_0^\infty \text{Re}\big[F(\text{i}\omega)\big]\text{d}\omega. \tag{6.60}$$

Note that the modification of the path of integration from one parallel to the real axis into one parallel to the imaginary axis is quite useful for making the numerical calculations efficient. This is because $\text{Im}\,F(z)$ is an oscillating function of $\text{Re}(z)$ on the path shown in Fig. 6.22, while $\text{Re}\,F(z)$ is a monotonically decreasing function along the imaginary axis on the path shown in Fig. 6.23a. Consequently, the number of mesh points needed in the calculation is strongly reduced after a suitable transformation of the integration variable.

In Shimizu *et al.* (1989) and Shimizu and Broglia (1990), pairing correlations in rapidly rotating nuclei have been studied using the general method discussed above. In these references, in addition to the RPA correlation energy, another measure of pairing correlations was introduced, namely the RPA pairing gap, Δ_{RPA} (called the 'effective' pairing gap). It is defined as

$$\Delta_{\text{RPA}} \equiv \sqrt{\Delta^2 + \tfrac{1}{2}G^2\,S_0(\text{RPA})}, \tag{6.61}$$

with

$$S_0(\text{RPA}) \equiv \sum_{n \neq \text{AGN}} \Big[|\langle n|P|0\rangle|^2 + |\langle n|P^\dagger|0\rangle|^2\Big]_{\text{RPA}}, \tag{6.62}$$

where $\Delta = G\,\langle 0|P^\dagger|0\rangle_{\text{HB}}$ is the standard, static BCS pairing gap (the order parameter of mean field), while G is the pairing force strength. The non-energy

weighted sum rule S_0(RPA) describes the contribution of pairing fluctuations, associated with the monopole pair-transfer operator, $P^\dagger = \sum_{i>0} a_i^\dagger a_{\bar{i}}^\dagger$, to the effective (RPA) gap. Note that $\sum_{n \neq AGN}$ means that the divergent contribution from the zero energy mode (pairing rotation) is to be excluded, in keeping with the fact that its contribution to equation (6.61) is included through the static (BCS) pairing gap Δ. In Shimizu *et al.* (1989), S_0(RPA) was calculated making use of the expression

$$S_0(\text{RPA}) \approx \frac{1}{\pi} \int_{\omega_{\text{cut}}}^{\infty} \text{Im Tr}\big[\mathcal{R}(\omega + i\varepsilon)\big]d\omega, \qquad (6.63)$$

where $\mathcal{R}(\omega) \equiv \mathcal{R}^{(\lambda=1)}(\omega)$ is the RPA response function, whose dimension is 2 corresponding to $Q_1 = (P^\dagger + P)/\sqrt{2}$ and $Q_2 = i(P^\dagger - P)/\sqrt{2}$. A finite value of ε and a low-energy cutoff ω_{cut} are used to get rid of the AGN mode contribution numerically. This is the same approximation as that used in calculating the RPA correlation energy, and can then be avoided using the path shown in Fig. 6.23(b). In this way one avoids the singularity associated with an eventual zero mode, as
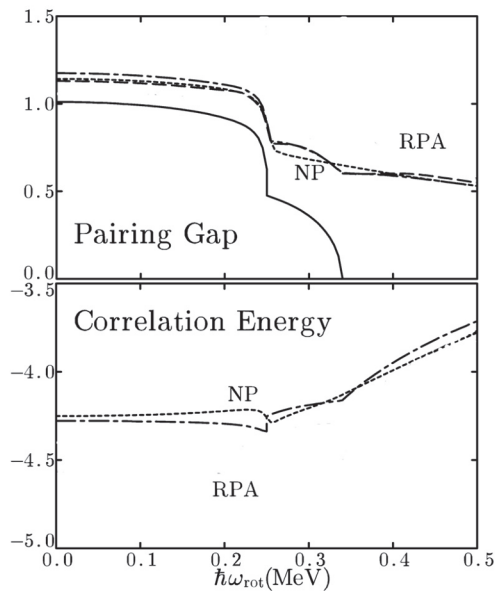
Figure 6.24. RPA pairing gap (upper panel) and RPA correlation energy (lower panel) for neutrons in ^{164}Er as a function of the rotational frequency. Both quantities are in MeV. The dash-dotted curves denote the results of calculations with $\varepsilon = 200\,\text{keV}$ and $\hbar\omega_{\text{cut}} = 400\,\text{keV}$. The value of the static (mean-field) pairing gap Δ, which vanishes at $\hbar\omega_{\text{rot}} = 0.34\,\text{MeV}$, is also displayed in the upper panel (continuous curve). The results of the number-projection (NP) calculations are shown as dotted curves.

in this case $\mathcal{R}(z)$ has a second-order pole at the origin (see Donati *et al.* (1999a)):

$$S_0(\text{RPA}) = \frac{1}{\pi} \int_0^\infty \text{Re Tr}\big[\mathcal{R}(a + i\omega)\big]d\omega. \qquad (6.64)$$

Since the function $\text{Tr}\big[\mathcal{R}(z)\big]$ has poles as singularities, the integral is independent of the choice of a. Summing up, making use of equations (6.60) and (6.64), both the RPA correlation energy and the RPA pairing gap can be exactly evaluated in a numerically efficient way.

In Fig. 6.24 we compare the results of the exact and approximate calculations of both $E_{\text{corr}}^{\text{RPA}}$ and Δ_{RPA} in the case of deformed, superfluid nuclei as a function of the rotational frequency. The average correlation energy is -4 MeV. This is much larger than the BCS pair correlation energy (≈ -1.5 MeV) calculated in Section 3.5. The difference is the RPA correlation energy (see also Section 8.4).

There is another method which allows us to go beyond mean-field approximation, namely the number-projection (NP) (see e.g. Ring and Schuck (1980), see also Section 4.2.2, in particular equation (4.45)). In Fig. 6.24 we also included the NP results for comparison. The NP correlation energy is defined as the energy difference between the NP and mean field (Hartree–Bogoliubov), $E_{\text{corr}}^{(\text{NP})} \equiv E_{\text{NP}} - E_{\text{HB}}$ (the exchange energy is included in E_{NP}). Although RPA leads to larger values of the correlations, especially in the superfluid phase, the rotational frequency dependences are quite similar. The advantage of the NP method over the RPA is to lead to smooth functions for both the correlation energy and the pairing gap at the pairing phase-transition point.

Pairing vibrations in the RPA framework have also been considered in the phase transition of metallic clusters as a function of temperature (see Fig. 1.15 and Mühschlegel *et al.* (1972), Lauritzen *et al.* (1993)). Within this context, it is of interest to consider the effect the dynamical pairing gap (see also Dang and Arima (1998, 2003)) may have on the width of the giant dipole resonance at low temperature (see N. Dinh Dang and A. Arima, *Key Topics in Nuclear Structure*, Paestum, 23–27 May, 2004, abstracts, p. 63).